Galvanic Interactions on Periodically Regular Heterogeneous Surfaces

A heterogeneous electrode surface has been modeled using a regular distribution of circular anodes in a surrounding coplanar cathodic matrix. In the absence of mass transport effects, galvanic currents and potentials have been calculated using finite-element analysis, with nonlinear electrode kinetics. For a fixed ratio of anodic to cathodic areas on a heterogeneous surface, calculated galvanic currents increase linearly with the active perimeter between cathodic and anodic regions. Furthermore, the current is independent of the shapes and distributions of anodic regions in a surrounding cathodic plane provided that the ratio of overall anodic area to active perimeter is conserved. Thus, due to its longer active perimeter, a surface represented by a large number of tiny anodic islands dispersed in a cathodic sea will exhibit much greater galvanic currents than an equivalent surface represented by a small number of large anodic continents.

Rael Morris, William Smyrl
Department of Chemical Engineering
and Materials Science
Corrosion Research Center
University of Minnesota
Minneapolis, MN 55455

Introduction

Heterogeneous surfaces are ubiquitously found in electrochemical systems and a systematic study of their behavior is essential to further our understanding of the many important phenomena that occur on these surfaces. In the electrochemical field several important electrode processes occur on heterogeneous surfaces, including: nonuniform galvanic corrosion (Isaacs and Ishikawa, 1985; Smyrl and Newman, 1976), reactions occurring on blocked electrodes (Hitzig et al., 1984; Rosner, 1966), noncoherent protective layers (Isaacs, 1986), electrocatalytic systems (Frank and Honda, 1982; Wright and Stroud, 1985), and arrays of microelectrodes (Reller et al., 1982). The transport behavior in all of these systems can be divided into two major categories:

1. Those in which reacting species are being transported through the electrolyte between a heterogeneous electrode surface and a counterelectrode
2. Those in which species are transported through the electrolyte between different parts of the same heterogeneous surface

In the former category, systems can be analyzed without taking into account the details of the surface geometry. The latter, however, requires a more detailed accounting of the surface geometry, because in these cases it is the surface geometry which defines the transport paths of the active species.

Galvanic corrosion occurs when two dissimilar metals in electrical contact are immersed in an electrolytic solution. Upon immersion in the electrolyte each metal attains a different equilibrium rest potential with respect to a reference electrode placed in the electrolyte. The difference in rest potentials manifests itself as a driving force for electron flow if the metals come into electrical contact. The metal having the lowest rest potential experiences an accelerated dissolution process as a result of this electron flow (referred to as galvanic current) and is called the anode; the other metal is the cathodic partner (Fontana and Greene, 1978). Galvanic corrosion systems fall into the category of systems in which different parts of the same surface interact with one another (Smyrl, 1981b), but they have been treated in the literature with simplified assumptions regarding the structure of the surface geometry. It has been only very recently, with easy access to large digital computing facilities, that more realistic geometric models have been used. We will use terminology and language descriptive of galavanic corrosion in the work presented here, but the generalization to other systems should be apparent.

Although there is a host of literature pertaining to current and potential distributions (Ibl, 1983), almost all the work that has been done has been in two-dimensional systems. The realistic representation of a heterogeneous surface electrode process necessitates the use of a three-dimensional geometric model; two dimensions are required to describe the surface geometry, while ionic current flows in the third dimension. Some three-dimensional modeling of potential distributions has appeared recently

in the literature, using either analytical or numerical techniques to solve the associated problem (Shih and Pickering, 1987; Zamani et al., 1986). Although analytical techniques are useful for predicting general trends, they are applicable in only the most simple of geometries and kinetic assumptions, and therefore cannot cover the very wide range of kinetic behavior or geometry expected to occur in real systems. In order to resolve three-dimensional problems, extremely powerful computational facilities are required. It is largely due to this fact that previous researchers have invariably gone to great lengths to simplify the geometry of interest in such a manner that it can be treated in a lower dimensionality.

The finite-difference technique has been used extensively in the electrochemical literature (Fleck et al., 1964) to solve the differential equations associated with the potential distribution problem; more recently the orthogonal polynomial collocation technique (Caban and Chapman, 1976) has been used. These techniques are difficult to use in situations where the geometry is not easily mapped into a regular domain, and has given way to the more popular variational technique of the boundary-element method (Brebbia, 1978; Hume et al., 1984) and the weighted residual finite-element method (Strang and Fix, 1973; Alkire et al., 1978). The boundary-element method is particularly useful for treating potential distributions in situations where mass transfer effects are not important. This method suffers the disadvantage of being difficult to adapt to solving coupled partial differential equations that arise in potential distribution problems that depend on diffusion effects. The finite-element method (FEM) can be applied to complex geometries, with the ability to handle any system of coupled nonlinear partial differential equations. In handling problems with increasing degrees of complexity the finite-element method affords the easy transition from a single differential equation to systems of coupled partial differential equations without having to make structural changes to the analytical process. The FEM was chosen here for the flexibility that it provides in adding additional complexity (reality) to the model equations.

The approach taken before this work has been to concentrate on a particular type of system geometry, and to make the analysis on the chosen geometry of interest. No previous systematic study has been performed to identify in a generic manner geometrical characteristics that determine the system behavior. The present contribution describes the general analysis of current and potential distributions on idealized heterogeneous surfaces, modeled as regular arrays of anodic islands in a surrounding cathodic plane. Full Butler-Volmer kinetics have been used, as well the associated linear approximation. Results are compared with those obtained on an annular disk-plane geometry. The major objectives here are to develop a basis on which to compare system behavior for different geometry types, and in so doing to enable simplified analysis of systems with complex geometrical configurations.

Model and Methods

Electrochemical transport equations and geometry

The current and potential distribution in an electrochemical system may be solved by considering the applicable transport equations. If the concentrations of all species are assumed to be uniform throughout the electrolyte, and electroneutrality is assumed, then the flux equation reduces to Ohm's law (Newman, 1973), which relates the current density to the gradient of the potential field:

$$\boldsymbol{i} = -\kappa \nabla \phi \tag{1}$$

The equation of continuity coupled with the electroneutrality assumption results in a conservaton equation for the current density:

$$\nabla \cdot \boldsymbol{i} = 0. \tag{2}$$

If the conductivity κ is further assumed to be uniform, then Laplace's equation results for the potential field:

$$\nabla^2 \phi = 0 \tag{3}$$

Thus in order to determine the current and potential distribution in an electrochemical system it is necessary to solve Laplace's equation for the potential. This cannot be done however without first defining the geometry of the system, as well as identifying boundary conditions to be used, *i.e.*, the charge-transport kinetics at the electrolyte/electrode interface (Smyrl, 1981a).

The heterogeneous surface is modeled as an array of anodic islands in a surrounding cathodic plane, with an anodic kinetic condition imposed on the normal gradient of the potential at the anode surface,

$$-\kappa \nabla \phi \cdot \boldsymbol{n} = i_0^A \left[e^{\alpha_{aa} n_a F / RT(\phi - v_A)} - e^{-\alpha_{ac} n_a F / RT(\phi - v_A)} \right] \tag{4}$$

and a corresponding cathodic condition applied on the cathodic plane,

$$-\kappa \nabla \phi \cdot \boldsymbol{n} = i_0^C \left[e^{\alpha_{ca} n_c F / RT(\phi - v_C)} - e^{-\alpha_{cc} n_c F / RT(\phi - v_C)} \right] \tag{5}$$

If the anodic islands are far enough apart, they can be considered isolated. Smyrl and Newman (1976) have solved the equations for this case. With finite spacing of the anodic islands, the problem can be solved on a symmetry element, whose geometry is determined by the entire array of islands. Moreover, across the boundary of each symmetry element an insulating condition applies, *i.e.*,

$$\boldsymbol{n} \cdot \nabla \phi = 0 \tag{6}$$

The insulating condition was also applied at the upper extremity of the domain, where the electrolyte solution reaches its maximum height, corresponding to the phase boundary between the electrolyte and the atmosphere. A typical smallest symmetry element (for a rectangular array of circular anodic islands) is shown in Figure 1.

The equations can be reformulated in dimensionless form by defining the following dimensionless variables:

$$\Phi = \frac{F}{RT}\phi \quad X = \frac{x}{l} \quad Y = \frac{y}{l} \quad Z = \frac{z}{l}$$

$$V_A = \frac{n_a F}{RT} v_A \quad V_C = \frac{n_c F}{RT} v_C \tag{7}$$

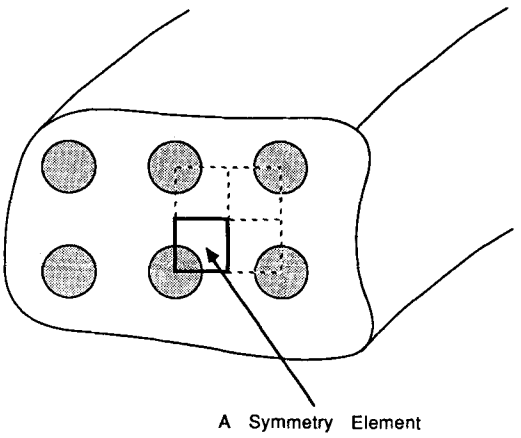

Figure 1. Symmetry element for a rectangular array of circular anodic islands.

where l is a characteristic length dimension for the system, which may be chosen here to be the radius of a circular island, but is shown to depend on other factors according to the geometry of interest.

The model equations may be written in Cartesian coordinates as follows:

$$\frac{\partial^2\Phi}{\partial X^2} + \frac{\partial^2\Phi}{\partial Y^2} + \frac{\partial^2\Phi}{\partial Z^2} = 0 \quad \text{in } \Omega \tag{8}$$

$$-\frac{\partial\Phi}{\partial Z} = J_A\left[e^{\alpha_{aa}(\Phi - V_A)} - e^{-\alpha_{ac}(\Phi - V_A)}\right] \quad \text{on } \partial\Omega_A \tag{9}$$

$$-\frac{\partial\Phi}{\partial Z} = J_C\left[e^{\alpha_{ca}(\Phi - V_C)} - e^{-\alpha_{cc}(\Phi - V_C)}\right] \quad \text{on } \partial\Omega_C \tag{10}$$

$$\boldsymbol{n}\cdot\nabla\Phi = 0 \quad \text{on } \partial\Omega_S \tag{11}$$

$$\left(\frac{\partial\Phi}{\partial Z}\right)_{Z=Z_{max}} = 0 \tag{12}$$

The dimensionless parameters J_A and J_C are defined by:

$$J_A = \frac{i_0^A Fl}{\kappa RT} \quad J_C = \frac{i_0^C Fl}{\kappa RT} \tag{13}$$

The Butler-Volmer kinetic expressions in Eqs. 9 and 10 are often linearized in order to simplify the analytical process. The result of linearizing Eqs. 9 and 10 yields:

$$-\frac{\partial\Phi}{\partial Z} = J_A(\alpha_{aa} + \alpha_{ac})(\Phi - V_A) \quad \text{on } \partial\Omega_A \tag{14}$$

$$-\frac{\partial\Phi}{\partial Z} = J_C(\alpha_{ca} + \alpha_{cc})(\Phi - V_C) \quad \text{on } \partial\Omega_C \tag{15}$$

The sums of the transfer coefficients $(\alpha_{aa} + \alpha_{ac})$ and $(\alpha_{ca} + \alpha_{cc})$ are often assumed to be unity, and Eqs. 14 and 15 are then reduced to:

$$-\frac{\partial\Phi}{\partial Z} = J_A(\Phi - V_A) \quad \text{on } \partial\Omega_A \tag{16}$$

$$-\frac{\partial\Phi}{\partial Z} = J_C(\Phi - V_C) \quad \text{on } \partial\Omega_C \tag{17}$$

Equations 8–13 fully describe the system to be solved, once the details of the geometry have been carefully defined and the kinetic parameters have been determined.

Several different geometric patterns were used to model the heterogeneous surface; they are represented in Figure 2. The simplest geometry corresponds to an annular representation of a hexagonal structure of regularly arranged circular anodes. The other two geometries represent arrays of either single-size or alternating size circular anodes in a rectangular array. In all cases the smallest symmetry elements were defined, with the insulating boundary condition, Eq. 11, applied to the symmetry planes $\partial\Omega_S$. The anodic condition, Eq. 9, was applied to the circular anodes $\partial\Omega_A$ located on the $Z = 0$ plane, and the cathodic condition, Eq. 10, applied to the cathodic plane $\partial\Omega_C$ also located in the $Z = 0$ plane. Finally, an insulating boundary condition, Eq. 12, was applied to the upper solution layer located at $Z = Z_{max}$.

Finite-element method

The finite-element method, known to be very efficient, accurate, and convenient for partial differential equations with irreg-

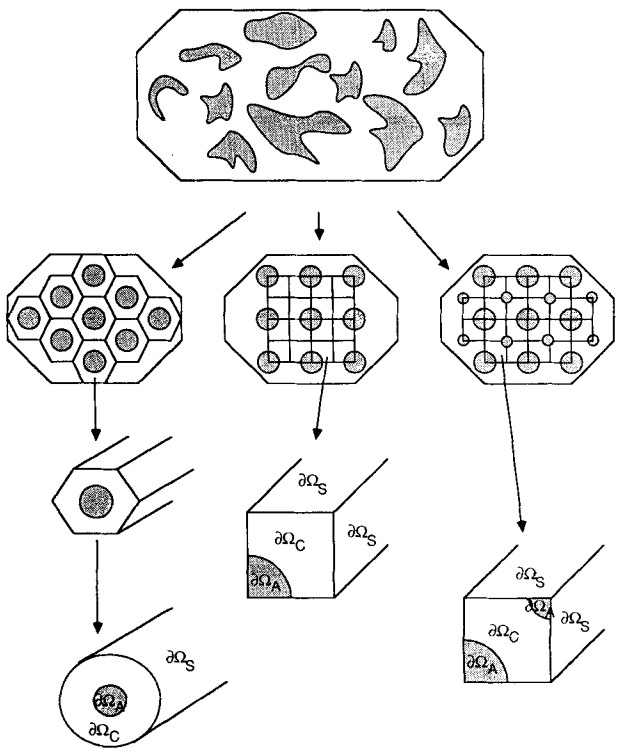

Figure 2. Types of regular approximations to a heterogeneous surface geometry.

ular domains, is used to solve Eqs. 8–13 for the various arrays considered. Because a true variational principle exists for our problem (Finlayson, 1972), the finite-element equations are generated by minimizing the functional:

$$I(\Phi) = \iiint_{\Omega} \left[\left(\frac{\partial\Phi}{\partial X}\right)^2 + \left(\frac{\partial\Phi}{\partial Y}\right)^2 + \left(\frac{\partial\Phi}{\partial Z}\right)^2\right] dX\,dY\,dZ + 2J_A \iint_{\partial\Omega_A} \left[\frac{e^{\alpha_{aa}(\Phi - V_A)}}{\alpha_{aa}} + \frac{e^{-\alpha_{ac}(\Phi - V_A)}}{\alpha_{ac}}\right] dX\,dY + 2J_C \iint_{\partial\Omega_C} \left[\frac{e^{\alpha_{ca}(\Phi - V_C)}}{\alpha_{ca}} + \frac{e^{-\alpha_{cc}(\Phi - V_C)}}{\alpha_{cc}}\right] dX\,dY \tag{18}$$

The functional in Eq. 18 represents the total energy associated with the potential field, and thus if the functional is minimized, the equilibrium potential field will be established, resulting in the solution to differential Eqs. 8–13.

A finite-element representation of the dimensionless potential Φ begins with division of the domain Ω of the governing equations into a convenient set of elements. The selection of the elements will depend on the geometry of the system to be investigated. The next step is to expand Φ with a set of basis functions $\{u^i\}$, $i = 1, \ldots, N$,

$$\Phi = \sum_{i=1}^{N} \psi_i u^i \tag{19}$$

where N is the number of nodes. Each of the basis functions u^i has the property that it is equal to unity at node i and zero at all remaining nodes. Thus the value of the coefficient ψ_i will be equal to the value of Φ at node i.

The conditions for a minimum of the functional $I(\Phi)$ are simply that the partial derivatives of Eq. 18 with respect to the coefficients ψ_i be zero:

$$\frac{\partial I(\Phi)}{\partial \psi_i} = 0 \tag{20}$$

which stated explicitly yields,

$$f_i(\Phi) = \iiint_{\Omega} \left[\left(\frac{\partial\Phi}{\partial X}\right)\left(\frac{\partial u^i}{\partial X}\right) + \left(\frac{\partial\Phi}{\partial Y}\right)\left(\frac{\partial u^i}{\partial Y}\right) + \left(\frac{\partial\Phi}{\partial Z}\right)\left(\frac{\partial u^i}{\partial Z}\right)\right] dX\,dY\,dZ + J_A \iint_{\partial\Omega_A} \left[e^{\alpha_{aa}(\Phi - V_A)} - e^{-\alpha_{ac}(\Phi - V_A)}\right] u^i\,dX\,dY + J_C \iint_{\partial\Omega_C} \left[e^{\alpha_{ca}(\Phi - V_C)} - e^{-\alpha_{cc}(\Phi - V_C)}\right] u^i\,dX\,dY = 0 \qquad i = 1, 2, \ldots, N \tag{21}$$

The set of Eqs. 21 is a nonlinear set of algebraic equations in the unknowns ψ_i. The identical set of equations is obtained by forming the Galerkin weighted residuals of Eqs. 8–13 with weighting functions $\{u^i\}$, $i = 1, 2, \ldots, N$. The motivation behind the use of the variational representation is that each of the terms in Eq. 18 can be given a physical interpretation.

In order to solve the system of nonlinear algebraic Eqs. 21, an iterative scheme has to be implemented. In our case it is very convenient to use the Newton-Raphson technique; *i.e.*, in order to solve $f_i(\Phi) = 0$, for $i = 1, \ldots, N$, for the unknowns ψ_i. In setting up this algorithm efficiently it should be noted here that the only entries of the Jacobian matrix that need to be recomputed during the iteration are those that correspond to nodes falling on the active boundaries ($\partial\Omega_A$ and $\partial\Omega_C$). This makes the implementation of a semi-Newton method extremely attractive (More and Cosnard, 1979), since successive Jacobian matrices are very similar to one another except for the entires corresponding to nodes on the active boundaries. Using the semi-Newton technique the Jacobian matrix is only evaluated and factored every fifth (approximately) iteration.

Geometry, coordinate systems, and mesh discretization

annular geometry

In an annular arrangement, the axial symmetry enables the problem to be reduced to two dimensions, with the polar coordinate system the most convenient to use. For the annular geometry, in polar coordinates, Eqs. 21 reduce to:

$$0 = \sum_{j=1}^{N} \psi_j \iint_{\Omega} (u^i_\rho u^j_\rho + u^i_z u^j_z)\,\rho\,d\rho\,dZ + J_A \int_0^{\rho_1} \left[e^{\alpha_{aa}(\Sigma_{k=1}^{N}\psi_k u^k - V_A)} - e^{-\alpha_{ac}(\Sigma_{k=1}^{N}\psi_k u^k - V_A)}\right] u^i\,\rho\,d\rho + J_C \int_{\rho_1}^{\rho_2} \left[e^{\alpha_{ca}(\Sigma_{k=1}^{N}\psi_k u^k - V_C)} - e^{-\alpha_{cc}(\Sigma_{k=1}^{N}\psi_k u^k - V_C)}\right] u^i\,\rho\,d\rho \qquad i = 1, 2, \ldots, N \tag{22}$$

The domain and its associated meshing scheme are represented in Figure 3. The domain is divided into quadrilateral elements with varying numbers of intervals in the ρ and Z directions, depending on the numerical accuracy desired. Each quadrilateral (ρ, Z) element is mapped isoparametrically onto the standard (ξ, η) unit square; all variables are interpolated using biquadratic basis functions in a standard implementation of the finite-element method (Dhatt and Touzot, 1985).

Regular array of single-size disks

In this case there is again no axial symmetry, and the full three-dimensional equations must be solved. It is most convenient in this case to work in cylindrical coordinates, and Eqs. 21

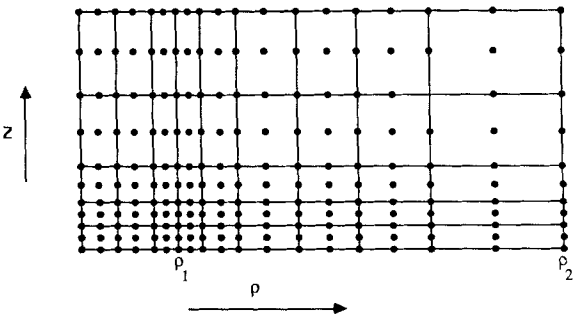

Figure 3. Meshing scheme and domain for annular geometry.
A polar coordinate system was chosen; elements used were nine-node biquadratics

become:

$$0 = \sum_{j=1}^{N} \psi_j \left[\iiint_{\Omega} \left(u_\rho^i u_\rho^j + \frac{1}{\rho^2} u_\theta^i u_\theta^j + u_z^i u_z^j \right) \rho \, d\rho \, d\theta \, dZ \right]$$
$$+ J_A \iint_{\partial\Omega_A} \left[e^{\alpha_{aa}(\sum_{k=1}^{N} \psi_k u^k - V_A)} - e^{-\alpha_{ac}(\sum_{k=1}^{N} \psi_k u^k - V_A)} \right] u^i \rho \, d\rho \, d\theta$$
$$+ J_C \iint_{\partial\Omega_C} \left[e^{\alpha_{ca}(\sum_{k=1}^{N} \psi_k u^k - V_C)} - e^{-\alpha_{cc}(\sum_{k=1}^{N} \psi_k u^k - V_C)} \right] u^i \rho \, d\rho \, d\theta$$
$$i = 1, 2, \ldots, N \qquad (23)$$

The domain in this case is represented in Figure 4. The domain is divided into curvilinear brick-shaped elements, with varying numbers of divisions in the three coordinate directions, depending on the accuracy desired. Each (ρ, θ, Z) element is mapped isoparametrically onto a standard (ξ, η, ζ) unit cube. The incomplete 20-node quadratic local basis functions were used for interpolation and finite-element expansion (Dhatt and Touzot, 1985).

Regular array of two alternating-size disks (disk-pair array)

In this case, as in the previous one, there is no axial symmetry and the full three-dimensional equations must be solved. It is most convenient in this case to work in Cartesian coordinates, since there is no convenient location on which to define the axis of a cylindrical coordinate system. In this case Eqs. 21 become:

$$0 = \sum_{j=1}^{N} \psi_j \left[\iiint_{\Omega} \left(u_X^i u_X^j + u_Y^i u_Y^j + u_Z^i u_Z^j \right) dX \, dY \, dZ \right]$$
$$+ J_A \iint_{\partial\Omega_A} \left[e^{\alpha_{aa}(\sum_{k=1}^{N} \psi_k u^k - V_A)} - e^{-\alpha_{ac}(\sum_{k=1}^{N} \psi_k u^k - V_A)} \right] u^i \, dX \, dY$$
$$+ J_C \iint_{\partial\Omega_C} \left[e^{\alpha_{ca}(\sum_{k=1}^{N} \psi_k u^k - V_C)} - e^{-\alpha_{cc}(\sum_{k=1}^{N} \psi_k u^k - V_C)} \right] u^i \, dX \, \mathrm{dY}$$
$$i = 1, 2, \ldots, N \qquad (24)$$

The domain in this case is represented in Figure 5. The domain is again divided into curvilinear brick-shaped elements, with varying numbers of divisions in the three coordinate directions, depending on the desired accuracy. Each (X, Y, Z) element is mapped isoparametrically onto a standard (ξ, η, ζ) unit cube. The incomplete 20-node quadratic elements are again utilized, and the standard interpolation scheme was implemented (Dhatt and Touzot, 1985).

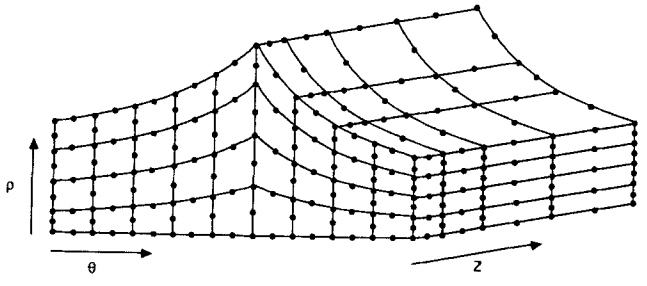

Figure 4. Meshing scheme and domain of smallest symmetry element for single-disk geometry.
A cylindrical coordinate system was chosen, with 20-node incomplete quadratic elements

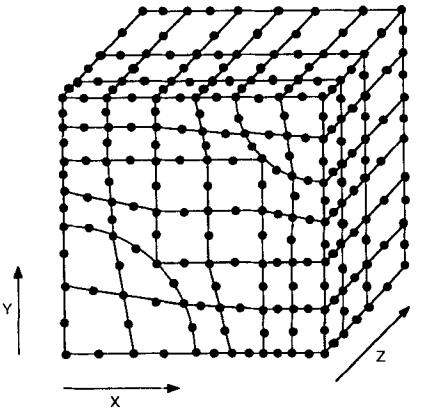

Figure 5. Meshing scheme and domain of smallest symmetry element for disk-pair geometry.
A rectangular coordinate system was chosen, with 20-node incomplete quadratic elements

Computation

All calculations were performed on the University of Minnesota Cray-2 Supercomputers. Finite-element programs were written to ensure to full vectorization of sections of the code that could be vectorized. Linear systems were solved using PCGPAK (Scientific Computing, 1987), a sparse matrix package that uses preconditioned conjugate gradient (PCG) algorithms. In our case an incomplete LU factorization was used to precondition our system. The PCG algorithm residual was reduced to 10^{-1} for Newton-Raphson (N-R) residuals in excess of 10^{-1}. When the N-R residual dropped below 10^{-1} the PCG residual was reduced to 10^{-8}. This decreased unnecessary work in solving the N-R linear system while the N-R iterate was far from the solution to the nonlinear system. During parameter exploration, zero-order continuation was used, which increased the speed of PCG and N-R convergence. CPU times for the calculations varied according to the size of the finite-element mesh, the number of iterations required for the Newton method to converge in the case of nonlinear problems, and the number of iterations performed in the PCG algorithm. Typical Cray-2 times varied from tens of seconds for the annular problem up to 10 min for a single refined mesh calculation performed for the two-disk problem.

Results and Discussion

The key issue is to compare the different geometries investigated with regard to their current and potential distributions and to generalize behavior for arbitrary geometrical configurations. Potential distributions are plotted in Figure 6. for the annular, single-disk, and disk-pair geometries. The qualitative behavior for all three geometries is very similar and also compares favorably to results previously reported for the annular geometry (McCafferty, 1975, 1977; Gal-Or et al., 1973). These qualitative similarities have been explored and numerical experiments have been devised to investigate the differences.

Potential and current distributions

In Figure 6 potential distributions have been plotted for the three different geometries investigated, for a specific choice of system parameters. The potential distributions have been represented by surfaces, with isopotential contours mapped onto a

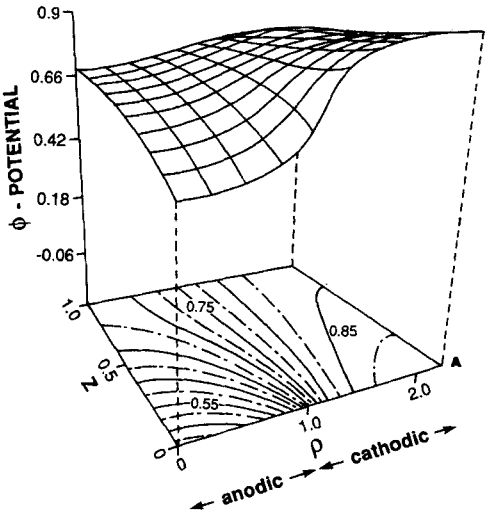

Figure 6a. Annular geometry.

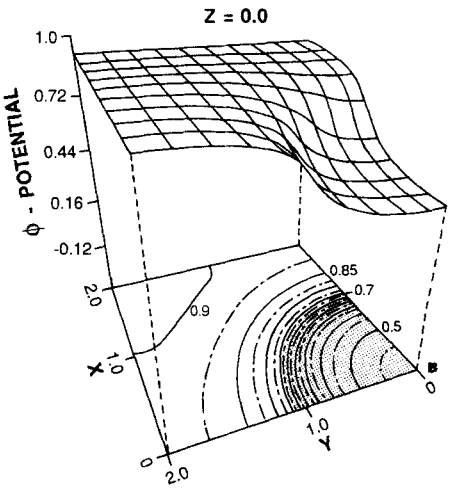

Figure 6b. Single-disk geometry.

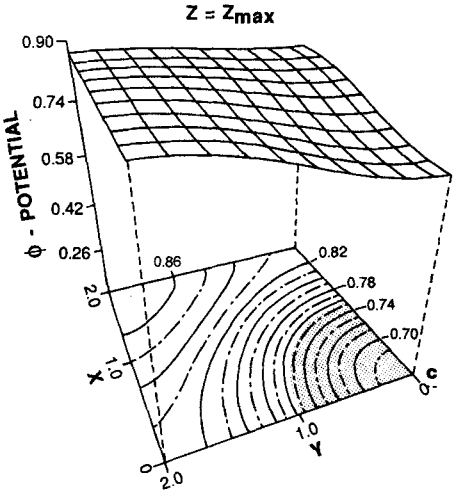

Figure 6c. Single-disk geometry.

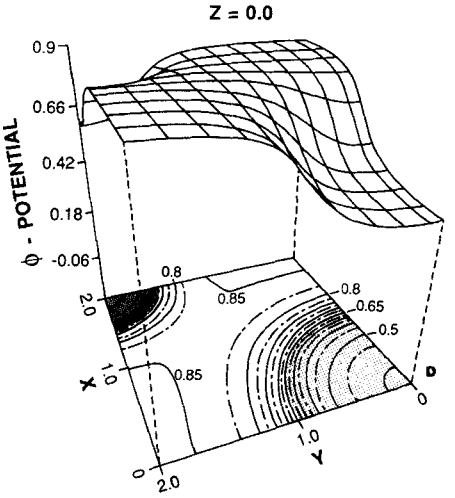

Figure 6d. Disk-pair geometry.

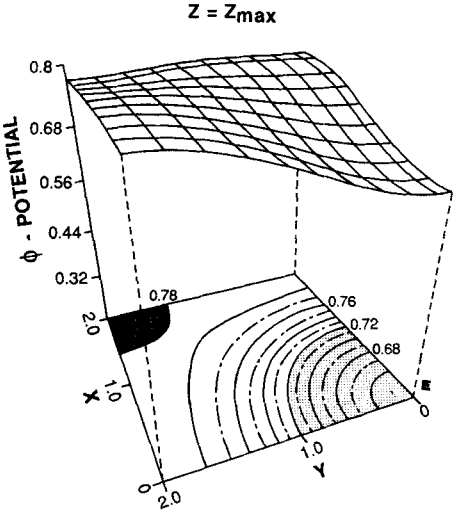

Figure 6e. Disk-pair geometry.

Figure 6. Potential distributions for all three geometries and $J_A = J_C = Z_{max}$.
Geometric parameters are given in Table 1 for all geometries.

plane below the potential surface. Results shown are for linear kinetics; in all cases $V_A = 0$, and $V_C = 1$, which represents a 26 mV difference in the rest potentials of the two metals for univalent corrosion reactions at room temperature.

For the annular geometry, it is possible to represent the entire domain in a two-dimensional surface representation as shown in Figure 6. This is not possible for the single-disk and disk-pair geometries; thus potential distributions have been included which represent the extremities of the domain (at $Z = 0$ and $Z = Z_{max}$).

In all of the results presented here, the distributions have very similar shapes as well as comparable quantitative values. In all geometries, the steepest slope of the potential surface exists in the near vicinity of the anode-cathode transition region. The results for the case of the annular geometry are identical to previous results for this configuration (McCafferty, 1975; McCafferty 1977). Based on the calculations shown in Figure 6 and additional calculations (not shown), the qualitative results can be summarized as follows:

1. Potential (current) distribution is more uniform at the electrode surface for larger values of electrolyte depth (Z_{max}).
2. The anode/cathode junction represents the most active region.
3. A uniform potential is reached far away from the electrode surface, with the farfield potential having a value close to the rest potential of:

- The least polarizable section of the electrode ($\partial\Omega_A$ if $J_A > J_C$ and *vice versa*)
- The section of the electrode having greatest area.

These could be opposing effects, in which case the farfield potential adopts some intermediate value relative to the electrode rest potentials.

These qualitative results are intuitive, and correspond to those obtained previously (McCafferty, 1975, 1977; Gal-Or et al., 1973). The results on all geometries are very similar, and it is this parallel behavior that has been exploited in the next section.

Active perimeter scaling for complex geometry

As a result of the locality of the potential gradient to the transition region between the anode and cathode, it was postulated that the total corrosion currents observed in these systems should scale with the length (perimeter) of the line tracing the boundary of the anode/cathode regions, which will be referred to as the active perimeter. To test this hypothesis, the alternating two-disk geometry was used in a numerical experiment, which kept the area ratios fixed but varied the active perimeter. This was done by allowing the two disks in this configuration to vary from equal size (maximum active perimeter) to the case where one disk is very much larger than the other (minimum active perimeter). It was found that the calculated corrosion current varied by as much as 50% with all kinetic parameters fixed, Figure 7. The key observation, however, is that the total *corrosion current varied in a linear fashion with the active perimeter.*

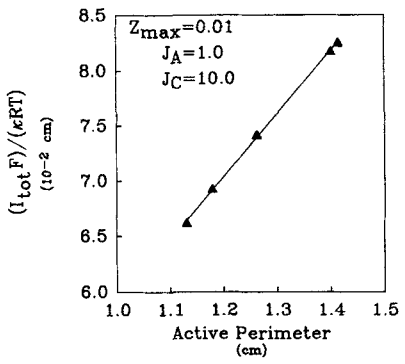

Figure 7. Effect of active perimeter on average corrosion current.
Typical system with equal anode/cathode areas, same linear polarization parameters, and same depth of electrolyte layer

The natural choice for the characteristic dimension in the annular and single-disk geometries is the radius of the anodic island. In keeping with this choice, and in attempting to include the active perimeter in the characteristic dimension of the system, l is chosen as:

$$l = \frac{2 \cdot \text{anode area}}{\text{active perimeter}} \tag{25}$$

The use of the active perimeter in scaling these systems follows the results of catalytic effectiveness calculations for similarly shaped catalytic island systems (Kuan et al., 1983a). The consequences of this choice for the characteristic dimension are summarized in Table 1 for all three geometries. In the case of the annular and single-disk geometry, the choice of l requires the

Table 1. Summary of Geometrical Parameters

Configuration	Required Parameters	Area Ratio $R = \frac{\text{anode area}}{\text{cathode area}}$	Chosen Parameters	Avg. Anodic Current Density
Annular	$\rho_1 = 1$	$\rho_2^2 - 1$	$\rho_2 = \frac{4}{\pi^{1/2}}$	$\frac{I_{tot}F}{\pi\kappa lRT}$
Single disk	$c = 1$	$\left(\frac{4}{\pi}\right)ab - 1$	$a = b = 2$	$\frac{4I_{tot}F}{\pi\kappa lRT}$
Disk pair	$\frac{c^2 + d^2}{c + d} = 1$	$\left(\frac{4}{\pi}\right)\left(\frac{ab}{c^2 + d^2}\right) - 1$	$a = b = 2^{1/2}x$ $c = [x^2 + x(4 - x^2)^{1/2}]/4$ $d = [x^2 - x(4 - x^2)^{1/2}]/4$ $2^{1/2} < x \leq 2$	$\frac{8I_{tot}F}{\pi x^2\kappa lRT}$

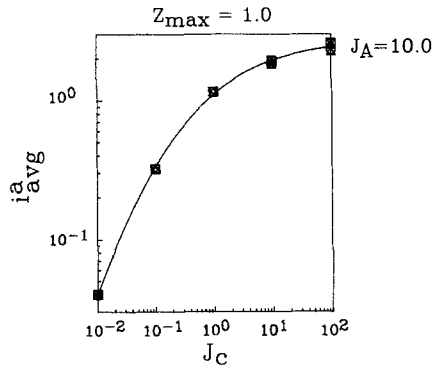

Figure 8. Typical results after scaling with active perimeter.
Universal curve for average anodic current for five geometries

radius of the anodic disk to be scaled to unit, while for the disk-pair geometry, a restriction is placed on the allowed values for the scaled anode radii. This choice for l also determines the expressions for the area ratio, R, as given in Table 1. ρ_1 and ρ_2 are the inner and outer radii in the annular geometry; a and b are the lengths of the sides of the rectangular symmetry elements; c and d represent radii of the anodic disks in the single-disk and disk-pair geometries.

The geometries so defined were used in a series of test calculations over a range of values for the kinetic parameters and solution depths. In the case of the disk-pair geometry the relative sizes of the two disks were also varied. The anode-cathode area ratios were held at a fixed value ($R = [16/\pi] - 1$) in all calculations. The exact values of the geometrical parameters chosen are given in Table 1, along with the resultant expression for the average anodic current density i^a_{avg} for each geometry. I_{tot} is the total anodic current, and x is a scaling parameter which alters the relative sizes of the two anodic disks while keeping the area

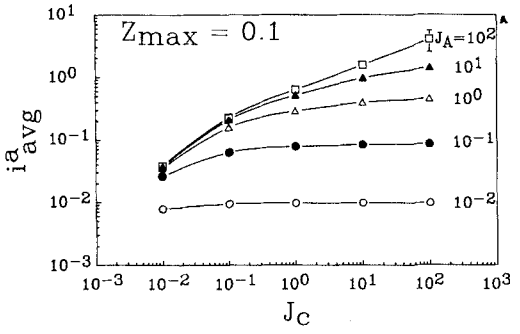

Figure 9a. Linear kinetics.

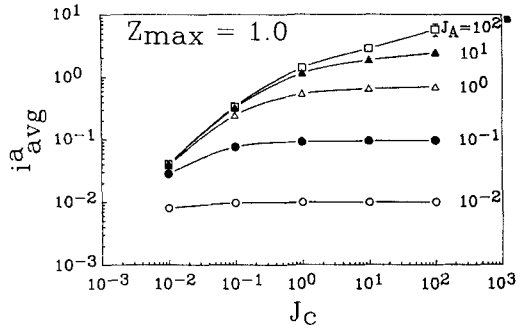

Figure 9b. Linear kinetics.

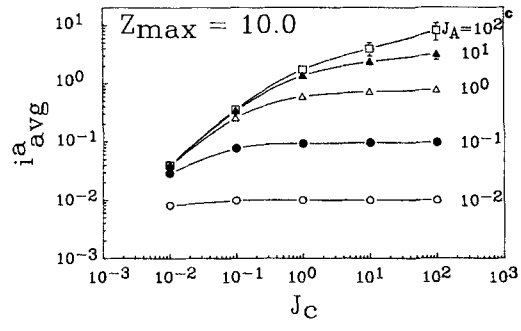

Figure 9c. Linear kinetics.

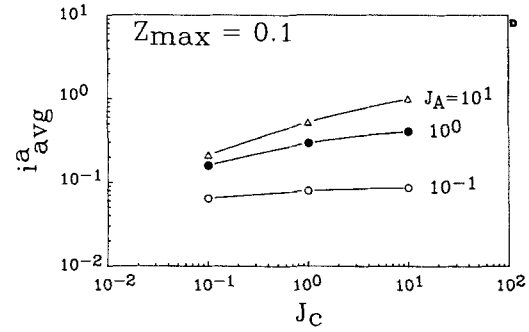

Figure 9d. Nonlinear kinetics.

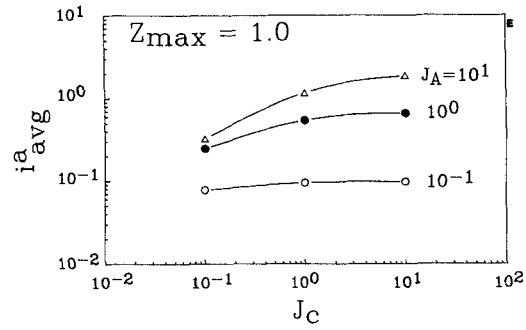

Figure 9e. Nonlinear kinetics.

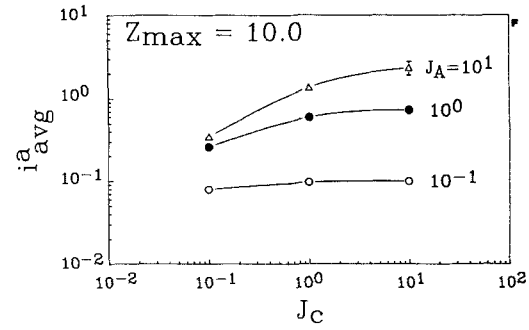

Figure 9f. Nonlinear kinetics.

Figure 9. Results for five geometries: median value of average anodic current density for each geometry; error bars indicate total range.

ratio and active perimeter fixed. As x approahces $\sqrt{2}$, one disk vanishes and the ratio of disk radii (c/d) approaches infinity. At the other limit, when $x = 2$ the two disks are of equal size.

In Figure 8, i^a_{avg} is plotted for five different geometrical configurations, corresponding to the annular, single-disk, and disk-pair geometries with $x = 1.5$, 1.7, and 1.9, respectively. The results presented in Figure 8 are typical and show a general trend for the corrosion current, independent of chosen geometry. The cases for which behavior deviates the most from this general trend are those in which the polarization parameters and total corrosion currents are large; there is strong evidence to suggest that a large amount of the scatter at these values is associated with differences in the grid sizes and meshing schemes used for the different geometries. The results for a wide range of system parameters are summarized in Figure 9, with the error bars indicating the scatter about the median value for the average anodic current density from all five chosen configurations. The typical deviation is within 2%. For the kinetic parameters chosen, the results of the nonlinear calculations are close to those made with the linear approximation.

The consequence of these results is that for arbitrary electrode configuration, the corrosion current may be estimated from knowledge of the active perimeter, and a calculation performed on a simple geometry (such as the annulus). These results also predict high values for the corrosion current for finely divided anodic and cathodic regions in a galvanically corroding system.

Conclusions

A model has been developed to examine the potential distribution in a hetrogeneous system of anodic islands in a coplanar cathodic matrix. Electrode kinetic behavior was modeled using full and linearized Butler-Volmer expressions. Systems studied include:

1. Annular arrangement of anode and cathode
2. Circular anodes in a square or rectangular array
3. Pairs of alternately sized anodes in a square or rectangular array, each circle being surrounded by four circles of the other kind

The finite-element method was used, and has been shown here to be a powerful and robust technique for handling nonlinear three-dimensional equations on regular geometries.

For a fixed ratio of anodic to cathodic areas on a heterogeneous surface, calculated galvanic current increases linearly with the active perimeter between cathodic and anodic regions. Furthermore, the current is independent of the shapes and distributions of anodic regions in a surrounding cathodic plane provided that the ratio of overall anodic area to active perimeter is conserved. Thus, due to its longer active perimeter, a surface represented by a large number of tiny anodic islands dispersed in a cathodic sea will exhibit much greater galvanic current than an equivalent surface represented by a small number of large anodic continents.

We have successfully developed a basis on which to compare system behavior for different geometry types by introducing a geometrically dependent characteristic dimension (the active perimeter). This enables the prediction of corrosion currents for complex systems using simple geometric configurations. We have used language and terminology descriptive of galvanic corrosion, but the results are equally applicable to mass, momentum, or energy transfer processes obeying identical conservation laws.

It is possible to determine the efficacy of the results in this paper for a more general class of surface geometries in which, for example, the anodic and cathodic regions may be randomly generated and dispersed in a plane using the Voronoi tessellation method (Kuan et al., 1983b; Winterfeld et al., 1981).

Acknowledgment

We are grateful to the Office of Basic Energy Sciences of the U.S. Department of Energy, Contract No. DE-FG02-88ER45338, and to the Minnesota Supercomputer Institute for financial support of this work.

Notation

a = length of side of symmetry element in single-disk and disk-pair geometries
b = length of other side of symmetry element in single-disk and disk-pair geometries
c = radius of single disk, or one of disk pairs in single-disk and disk-pair symmetry elements, respectively
d = radius of other disk in disk-pair symmetry element
f_i = nonlinear function of the potential Φ, representing the ith finite-element residual equation
F = Faraday constant, 96,485°C/mol
i = current density, A/cm^2
i = dummy counter for equations
i^A_0 = anodic exchange current density, A/cm^2
i^C_0 = cathodic exchange current density, A/cm^2
i^a_{avg} = average anodic current density
I = quadratic functional representing total energy associated with the potential field
I_{tot} = total anodic current, A
J_A = anodic polarization parameter
J_C = cathodic polarization parameter
l = characteristic length for system, cm
n_a = number of electrons transfered in anodic process
n_c = number of electrons transfered in cathodic process
N = number of finite-element euqations
$\boldsymbol{n}$ = unit normal vector
R = universal gas constant, 8.3143 J/mol · K
T = absolute temperature, K
u^i = ith basis function in finite-element expansion
V_A = anodic rest potential, V
V_C = cathodic rest potential, V
V_A = anodic rest potential
V_C = cathodic rest potential
x = coordinate direction, cm
x = geometric scaling parameter for disk-pair geometry
X = dimensionless coordinate direction
y = coordinate direction, cm
Y = dimensionless coordinate direction
z = coordinate direction, cm
Z = dimensionless coordinate direction
z_{max} = upper extremity of solution domain

Greek letters

α_{aa} = anodic transfer coefficient for anodic reaction
α_{ac} = cathodic transfer coefficient for anodic reaction
α_{ca} = anodic transfer coefficient for cathodic reaction
α_{cc} = cathodic transfer coefficient for cathodic reaction
$\partial\Omega$ = three-dimensional region representing entire domain
$\partial\Omega_A$ = two-dimensional anodic region on electrode surface
$\partial\Omega_C$ = two-dimensional cathodic region on electrode surface
$\partial\Omega_S$ = two-dimensional region representing symmetry plane
ϕ = solution potential, V
Φ = dimensionless solution potential
κ = solution conductivity, $\Omega^{-1} \cdot cm^{-1}$
ψ_i = coefficients in finite-element expansion
ρ = radial coordinate direction
ρ_1 = radius of inner circle in annular geometry

ρ_2 = radius of outer circle in annular geometry
θ = angular coordinate direction in single-disk geometry

Literatured Cited

Alkire, R., T. Bergh, and R. L. Sani, "Predicting Electrode Shape Change with Use of Finite-Element Methods," *J. Electrochem. Soc.*, **125,** 1981 (1978).

Brebbia, C. A., *The Boundary Element Method for Engineers,* Wiley, New York (1978).

Caban, R., and T. W. Chapman, "Rapid Computation of Current Distribution by Orthogonal Collocation," *J. Electrochem. Soc.*, **123,** 1036 (1976).

Dhatt, G., and G. Touzot, *The Finite-Element Method Displayed,* Wiley, New York (1985).

Finlayson, B. A., *The Method of Weighted Residuals and Variational Principles,* Academic Press, New York (1972).

Fleck, R. N., D. N. Hanson, and C. W. Tobias, "Numerical Evaluation of Current Distribution in Electrochemical Systems," UCRL-11612, Lawrence Radiation Lab., Berkley, CA (Sept., 1964).

Fontana, M. G., and N. D. Greene, *Corrosion Engineering,* 2nd ed. McGraw-Hill Series in Materials Science and Engineering, McGraw-Hill, New York (1978).

Frank, A. J., and K. Honda, "Visible-Light-Induced Water Cleavage and Stabilization of n-Type CdS to Photocorrosion with Surface-Attached Polypyrrole-Catalyst Coating," *J. Phys. Chem.*, **86,** 1933 (1982).

Gal-Or, L., Y. Raz, and J. Yahalom, "Mathematical Characterization of Corrosion Currents in Local Electrolytic Cells," *J. Electrochem. Soc.*, **120,** 598 (1973).

Hitzig, J., J. Titz, K. Juttner, W. J. Lorenz, and E. Schmidt, "Frequency Response Analysis of the Ag/Ag^+ System: A Partially Active Electrode Approach," *Electrochimica Acta,* **29,** 287 (1984).

Hume, E. C., III, W. M. Deen, and R. A. Brown, "Mass Transfer Analysis of Electrodeposition Through Polymeric Masks," *J. Electrochem. Soc.*, **131,** 1251 (1984).

Ibl, N., "The Current Distribution," *Comprehensive Treatise on Electrochemistry,* **3,** Ch. 4, J. O'M. Bockris et al., eds., Plenum, New York (1983).

Isaacs, H. S., "Detection of Defects in Ion Vapor Deposited Aluminum on Steel," Paper 194, *NACE Corrosion/86* (1986).

Isaacs, H. S., and Y. Ishikawa, "Applications of the Vibration Probe to Localized Current Measurements," Paper 55, *NACE Corrosion/85* (1985).

Kuan, D.-Y., H. T. Davis, and R. Aris, "Effectiveness of Catalytic Archipelagos. I: Regular Arrays of Regular Islands," *Chem. Eng. Sci.*, **38,** 719, (1983a).

———, "Effectiveness of Catalytic Archipelagos. II: Random Arrays of Random Islands," *Chem. Eng. Sci.*, **38,** 1569, (1983b).

McCafferty, E., "Mathematical Analysis of Current in Corrosion Cells with Circular Geometry," Naval Res. Lab. Rept. No. 7835, Washington, D.C. (1975).

———, "Distribution of Potential and Current in Circular Corrosion Cells Having Unequal Polarization Parameters," *J. Electrochem. Soc.*, **124,** 1869 (1977).

More, J. J., and M. Y. Cosnard, "Numerical Solution of Nonlinear Equations," *ACM Trans. Math. Software,* **5,** 64 (1979).

Newman, J., *Electrochemical Systems, Prentice-Hall, Englewood Cliffs, NJ (1973).*

Reller, H., E. Kirowa-Eisner, and E. Gileadi, "Ensembles of Microelectrodes, Digital Simulation," *J. Electroanal. Chem.*, **138,** 65 (1982).

Rosner, D. E., "Reaction Rates on Partially Blocked Rotating Disk—Effect of Chemical Kinetic Limitations," *J. Electrochem. Soc.*, **113,** 624 (1966).

Scientific Computing Associates, "PCGPAK User's Guide," Version 1.03, New Haven, CT (1987).

Shih, H., and H. W. Pickering, "Three-Dimensional Modeling of the Potential and Current Distributions in an Electrolytic Cell," *J. Electrochem. Soc.*, **134,** 551 (1987).

Smyrl, W. H., "Current and Potential Distributions in Corrosion Systems," *Lectures in Electrochemical Engineering, AIChE Symp. Ser.*, 77(204), 152 (1981a).

———, "Electrochemistry and Corrosion on Homogeneous and Heterogeneous Metal Surfaces," *Comprehensive Treatise of Electrochemistry,* **4,** J. O'M. Bockris et al., eds., Plenum, New York (1981b).

Smyrl, W. H., and J. Newman, "Current and Potential Distributions in Plating Corrosion Systems," *J. Electrochem. Soc.*, **123,** 1423 (1976).

Strang, G., and G. J. Fix, *An Analysis of the Finite-Element Method,* Prentice-Hall, Englewood Cliffs, NJ (1973).

Wright, D. C., and D. Stroud, "A Percolation Model for Electrocatalysis on Microparticle Electrodes," *J. Electrochem. Soc.*, **132,** 1507 (1985).

Winterfeld, P. H., L. E. Scriven, and H. T. Davis, "Percolation and Conductivity of Random Two-Dimensional Composites," *J. Phys. C,* **14,** 2361 (1981).

Zamani, N. G., J. F. Porter, and A. A. Mufti, "A Survey of Computational Efforts in the Field of Corrosion Engineering," *Int. J. Numer. Methods Eng.*, **23,** 1295 (1986).

Manuscript received Aug. 31, 1987, and revision received Dec. 29, 1987.